

Universal plaquette resistance of the cuprate superconductors

N. Barišić^{1,2,3,4*}, Y. Li⁵, G. Yu¹, X. Zhao^{1,6}, M. Dressel², A. Smontara³, M. Greven^{1*}

¹ School of Physics and Astronomy, University of Minnesota, Minneapolis, Minnesota 55455, USA

² 1. Physikalisches Institut, Universität Stuttgart, D-70550 Stuttgart, Germany

³ Institute of Physics, Bijenička c. 46, HR-10000 Zagreb, Croatia

⁴ Service de Physique de l'Etat Condensé, CEA-DSM-IRAMIS, F 91198 Gif-sur-Yvette, France

⁵ International Center for Quantum Materials, School of Physics, Peking University, Beijing 100871, China

⁶ State Key Lab of Inorganic Synthesis and Preparative Chemistry, College of Chemistry, Jilin University, Changchun 130012, China

* Correspondence to: nbarisic@ifs.hr, greven@physics.umn.edu

In the enigmatic lamellar cuprates, strong electronic correlations give rise to an insulating parent state from which superconductivity and eventually a Fermi-liquid-like metal emerge upon doping. At intermediate hole concentrations (p), the deviation from a linear-in-temperature planar resistivity ($\rho \propto T$) upon cooling toward the superconducting state is associated with the opening of a ‘pseudogap’ in the antinodal regions of the Fermi surface. Contrary to common belief, we find in the pseudogap phase of structurally simple $\text{HgBa}_2\text{CuO}_{4+\delta}$ that $\rho \propto T^2$, as in the putative Fermi-liquid state at high doping. By combining these results with prior work for other cuprates, we are able to obtain the fundamental resistance per copper-oxygen plaquette in both the linear ($\rho_{\square} = A_{1\square} T$) and quadratic ($\rho_{\square} = A_{2\square} T^2$) regimes, with $A_{1\square} \propto A_{2\square} \propto 1/p$. Any theory for the cuprates can now be benchmarked against this simple universal behavior of the planar resistivity.

When exploring the physical properties of a material, the resistivity is the quantity that is often first measured, but last understood. It is an observable that corresponds to a weighted integration over the whole Fermi surface (see supporting online material (SOM) a). Consequently, the resistivity is highly sensitive to changes in the electronic behavior of a system, and hence regularly used to detect phase transitions and to determine phase diagrams. Yet for the same reason, the resistivity typically exhibits complex temperature, magnetic field, etc., dependences. Nevertheless, when simple temperature dependences are observed, such as power-law in a metal or exponential in a semiconductor, this usually provides important insight into the fundamental properties of a system. Only in rare cases, such as the quantum Hall effect in correlated two-dimensional electron systems, has the magnitude of the resistivity been found to be the same for an entire class of materials.

Soon after the discovery of superconductivity in the cuprates a quarter of a century ago it was contended (1) that conventional phonon interactions cannot account for the unprecedentedly high transition temperatures (T_c). Instead it was argued that the close proximity to the Mott insulator implies a purely electronic mechanism. Yet despite intensive research, the peculiar metallic state from which superconductivity emerges at intermediate hole concentrations is still not understood. Here we first report quantitative measurements of the dc resistivity along the copper-oxygen planes of the structurally simple single-CuO₂-layer compound HgBa₂CuO_{4+δ} (Hg1201). For temperatures above the pseudogap temperature T^* (2, 3), we observe the well-known linear behavior $\rho = A_1 T$. Surprisingly, upon further cooling, we observe a distinct switch to a purely quadratic dependence, $\rho = A_2 T^2$, which holds between the lower characteristic temperature T^{**} and the onset of superconducting fluctuations at T' , just above T_c ($T^* > T^{**} > T' > T_c$). We then present a systematic analysis of prior data for double-layer YBa₂Cu₃O_{6+δ} (YBCO) (4, 5, 6, 7, 8, 9) as well as single-layer La_{2-x}Sr_xCuO₄ (LSCO) (5, 6, 10, 11, 12, 13) and Tl₂Ba₂CuO_{6+δ} (Tl2201) (10, 14). Due to the quasi-two-dimensional electronic structure of the cuprates, with its underlying square-planar CuO₂ sheets, it is natural to consider the resistance ρ_{\square} per Cu-O plaquette (SOM b), although this is rarely done. Across a large

part of the phase diagram, we demonstrate for all four compounds that the plaquette resistance coefficients $A_{1\Box}$ and $A_{2\Box}$ are universally proportional to the inverse hole concentration: $A_{1\Box} \propto A_{2\Box} \propto 1/p$. Our simple and entirely model-free analysis of the planar dc resistivity gives profound insight into the phase diagram and the nature of the conducting states of the high- T_c cuprates.

We prepared Hg1201 crystals according to a previously reported procedure (15, 16). The ab -plane dc resistivities of three underdoped samples with $T_c = 80$ K are displayed in Fig. 1A, and the magnetization characterization for one of them is shown in Fig. 1B. Since the samples are cleaved, their shapes are irregular, and consequently the absolute value of the resistivity ($\rho \approx 0.6$ m Ω cm at 300 K) could only be determined with about 20% accuracy (see SOM c for experimental methods and detailed results for other hole concentrations). However, regardless of their significantly different dimensions (e.g., a - b dimensions vary between about 0.01 and 1 mm), the samples exhibit identical temperature dependences (Fig. 1C) and, hence, a high degree of homogeneity. Extrapolation of the high-temperature linear behavior ($\rho = \rho_0 + A_1T$) to zero temperature gives $T^* \approx 280$ K and reveals a negligible residual resistivity. Such a small ρ_0 is usually taken as the signature of a clean metallic system, free of extrinsic and intrinsic disorder. This is noteworthy, since the underdoped cuprates typically exhibit a large ρ_0 , which increases with decreasing doping (3, 17).

The quadratic temperature regime is demonstrated in Fig. 1D. In the $T_c = 80$ K samples, it is found below $T^{**} \approx 170$ K and spans about 80 K in temperature before the influence of superconducting fluctuations is noticeable at T' . As shown in Fig. 2A-C, this behavior is also observed at lower doping (samples with $T_c = 47$ K and 67 K). In both the linear and quadratic temperature regimes, the residual resistivity is negligible in simple tetragonal Hg1201. In other compounds, ρ_0 can be substantial and the underlying quadratic behavior tends to be masked, although as shown in Fig. 2, it was previously observed for underdoped YBCO (between $p = 0.03$ and 0.09) (5, 7, 8), underdoped LSCO (for $p = 0.02$ and 0.08) (5), as well as strongly overdoped LSCO ($p = 0.33$), which is thought to

be a Fermi liquid (13). In Figs. 2E and SOM d, we demonstrate that this is even the case for prior data for LSCO at $p = 0.01$ (6). Tl2201 at $p \approx 0.30$ it is in close proximity to the putative Fermi-liquid regime, since the description of the temperature dependence of the planar resistivity requires only a small linear component (Fig. 2I) (10). In one measurement of YBCO ($p \approx 0.11$), superconductivity was suppressed by a 55 T magnetic field and $\rho \propto T^2$ was observed down to very low temperature (9). In Fig. 3B and SOM e, we demonstrate that the four characteristic temperatures and the underlying (zero-field) quadratic resistive regimes of YBCO, LSCO and Bi2201 can also be identified from prior contour plots of the second temperature derivative of the resistivity (17).

Hg1201 and YBCO are structurally very different compounds, with one and two CuO_2 planes per unit cell, respectively. However, as shown in Fig. 3, the doping-dependent temperatures T^* , T^{**} , T' and T_c determined from resistivity, which demarcate five distinct physical regions, are very similar. In both compounds, the opening of the pseudogap at T^* has been shown to be associated with a phase transition to a novel magnetically ordered state (18). The onset of the quadratic resistivity below T^{**} agrees surprisingly well with characteristic temperatures determined by two other probes: the peak in the thermoelectric power (TEP) for both Hg1201 (19) and YBCO (20, 21), and the onset of a Kerr rotation signal for YBCO, indicative of broken time-reversal symmetry (22). Similar to dc resistivity, TEP is derived from integrals over electronic states near the Fermi level (SOM a). Superconducting fluctuations affect the dc-conductivity only near T_c .

We now analyze the doping dependences of the linear and quadratic contributions to the plaquette resistance for Hg1201, YBCO (4, 5, 7, 8, 9), Tl2201 (10, 14) and LSCO (5, 6, 10, 11, 12). As shown in Figs. 3&4, three primary regions need to be distinguished: the T -linear regime ($p < p^* \approx 0.20$ and $T > T^*$) and the two quadratic regimes ($p < p^*$ and $T < T^{**}$; $p > 0.30$ and $T < 55$ K). For hole concentrations just above p^* , we have to rely largely on the available transport data for LSCO. In this doping range, LSCO is known to

be rather inhomogeneous (11), its low-temperature planar resistivity exhibits both linear and quadratic components (10, 11), and the role of inhomogeneities is not yet clear.

For numerous reasons, the doping dependences of $A_{1\Box}$ and $A_{2\Box}$ presented in Fig. 4 are remarkable. *First*, their values are universal, despite substantial differences in crystal structure, disorder, and optimal T_c of the four compounds (23). Consequently, the states near the Fermi level that contribute to the planar transport are essentially identical, and the underlying *ab*-plane resistivity in the normal state of the cuprates is now known. *Second*, $A_{1\Box}$ (for $p < p^*$) and $A_{2\Box}$ (except perhaps near p^*) are approximately proportional to the inverse hole concentration. *Third*, the scattering mechanism responsible for the linear temperature dependence of the resistivity is clearly related to fluctuations that disappear upon cooling below T^* and doping beyond p^* . This is apparent from the fact that $\rho \propto T$ is observed only above T^* , and also from the behavior of the resistivity just above p^* (Fig. 4B), where $A_{1\Box}$ decreases faster than $1/p$ and approaches zero around $p = 0.30$. *Fourth*, in underdoped Hg1201, we observe a dramatic ‘switch’ of scattering mechanisms: there is no discernible quadratic (linear) contribution above T^* (between T^{**} and T' and). *Fifth*, as already previously noted (6), the metallic behavior extends into the Néel state and nearly all the way to the undoped Mott insulator. From prior data for LSCO (6), we show that $\rho \propto T^2$ even at 1% doping (Fig. 2 and SOM d).

We now consider several possible interpretations of our findings. Based on the prior observation of metallic resistive behavior at low hole concentrations, a real-space picture of mesoscopic phase segregation was proposed, with a doping-dependent change of the effective volume relevant to charge transport (6). However, the evidence for such phase segregation in different cuprate families is varied, which appears difficult to reconcile with the observation of universality over a wide doping range presented in Fig. 4. Another viewpoint is that much of the cuprate phase diagram is controlled by an underlying quantum critical point (24, 25), which is supported by observations of novel magnetic order below T^* (18). In quantum-critical-point theories, the effective interactions among electrons, and consequently all single-particle renormalization

phenomena, are assumed to be controlled by a fluctuating order parameter of some kind. Scattering off such fluctuations for $T > T^*$ is proposed to cause the linear- T dependence of the resistivity. Interpreted in this fashion, the result in Fig. 4 indicates that, at low temperature, the critical fluctuations either condense below T^* ($p < p^*$) or gradually disappear ($p > p^*$).

A more specific picture is obtained by using the Drude formula $\rho = m^*/(ne^2\tau)$, which only assumes that it is possible to separate the scattering rate ($1/\tau$) from the effective density (n) of carriers (26). The observation of distinct power-law behaviors ($\rho_{\square} = A_{1\square}T$ and $A_{2\square}T^2$) over wide doping ranges suggests that the scattering rate is proportional to T and T^2 in the respective regions of the phase diagram. The simplest interpretation of the proportionality $A_{1\square} \propto A_{2\square} \propto 1/p$ then is to associate the doping dependence of the resistivity solely with the doped carriers: $n = p$. It follows that the respective scattering rates τ_1 and τ_2 as well as the band mass m^* are doping-independent and universal for all cuprates. This interpretation is consistent with prior experimental observations (6, 27, 28), such as the notion that the Fermi arc length in the pseudogap regime is proportional to p (28, 29). Furthermore, since $A_{1\square} \propto A_{2\square} \propto 1/p$ for $p < p^*$, the effective number of carriers would remain unaffected by the closing the pseudogap with increasing temperature, in contrast to the scattering rate. This would suggest that the predominant contribution to the conductivity at all temperatures comes from the relatively fast carriers (30, 31) in the nodal regions. Alternatively, one might invoke either the scattering off magnetic fluctuations (hot spots) associated with the antinodes or electronic scattering involving van Hove singularities near the Fermi surface (32). Finally, the antinodal states might be at the Planckian dissipation limit (11), beyond which coherent single particle propagation is inhibited (33, 34). The pseudogap formation might then be viewed as the lowering of the electronic energy in response to this intense scattering, preventing the scattering from remnant quasiparticle states into the ‘hot’ antinodal regions (11).

It is interesting to extend the above interpretation based on the Drude formula to the overdoped regime. Since $A_{2\Omega} \propto 1/p$ continues to hold below ~ 100 K well above p^* , it would seem that the number of carriers contributing to this term in the resistivity remains p and that the scattering rate $1/\tau_2$ remains unaffected by the closing of the pseudogap in the antinodal regions as the putative Fermi-liquid state at high doping is approached. On the other hand, quantum oscillation (35) and photoemission (36) experiments for overdoped Tl2201 indicate a large Fermi surface volume, which in accordance with Luttinger's theorem corresponds to $1 + p$ rather than p carriers. For Tl2201 at $p \approx 0.26$, a large magnetic field allowed the suppression of superconductivity, which revealed that in the zero-temperature limit the Wiedemann-Franz law is obeyed, and hence that the fermions that carry heat also carry charge e and the ground state is therefore indistinguishable from the Fermi-liquid (37). However, concomitantly, the planar resistivity contains a substantial T -linear term down to the lowest temperatures, a distinctly non-Fermi-liquid property. At $p \approx 0.30$, the low-temperature planar resistivity of Tl2201 still contains a small linear contribution (Figs. 2I and 4), and angle-dependent magnetoresistance measurements have been interpreted as indicative of two distinct scattering rates along the Fermi surface, with distinct temperature dependences (38). The appearance of the T -linear scattering rate has been linked with the onset of superconductivity with decreasing carrier concentration (11). Recent Raman scattering experiments for overdoped Tl2201 and double-layer $\text{Bi}_2\text{Sr}_2(\text{Ca}_{1-x}\text{Y}_x)\text{Cu}_2\text{O}_{8+\delta}$ report a well-defined mode with B_{1g} symmetry, consistent with a broken continuous symmetry (with unknown order parameter) at the onset of superconductivity, and it was speculated that this mode is related to the fluctuation spectrum at the origin of superconductivity (39). A purely Fermi-liquid-like quadratic resistivity has been observed for LSCO at $p = x = 0.33$, the highest doping level attained in the cuprates (13). Yet the Kadowaki-Woods ratio for LSCO ($p = 0.33$) was found to be significantly larger than for other correlated-electron systems (13). Clearly, the evolution toward the putative Fermi-liquid upon exiting the pseudogap state is intricate. Nevertheless, the simple proportionality $A_{2\Omega} \propto 1/p$ (except perhaps near p^*) shown in Fig. 4 demonstrates an intriguing connection between the underdoped and overdoped (purely T^2) regimes of the cuprate phase diagram.

Clarification of the nodal/antinodal dichotomy seems essential for understanding this connection.

It has been suggested that the underdoped cuprates are ‘nodal metals’ described by a two-component optical conductivity, with a low-energy Drude component that can be associated with coherent quasiparticles on the Fermi arcs observed in photoemission experiments (7, 27), and that the in-plane infrared spectral weight from optical conductivity is insensitive to the opening of the pseudogap at T^* (40). These results are consistent with our observations. Cluster dynamical mean-field calculations of the one-band Hubbard model at intermediate to strong coupling have been found to capture several aspects of the doping evolution, such as the nodal/antinodal momentum-space differentiation and the momentum selective pseudogap, but are constrained by the Fermion-sign problem and by limited momentum-space resolution (41). In three-band theories with O_x/O_y hopping and large Hubbard U_d on copper (34), the spectral weight in the nodal regions is associated primarily with planar oxygens, where the kinematic interaction generated by the large U_d and the direct Hubbard interaction on oxygens (U_p) are presumably weak. Consequently the nodal regions tend to be protected not only against magnetic correlations, as in the single-band Hubbard model (41), but also against incoherent Cu-O charge fluctuations within the unit cell. Since $A_{2\Box} \propto 1/p$ even at high hole concentrations, well outside the pseudogap regime, it is tempting to interpret the quadratic resistivity at all hole concentrations with the electronic scattering ($1/\tau_2 \propto T^2$) of a Fermi liquid, generalizing the Umklapp result for the Hubbard model (32). An alternative interpretation would be that the doping dependences of the scattering rates and carrier densities in the Drude expression compensate exactly in such a way that $A_{1\Box} \propto A_{2\Box} \propto 1/p$. However, in the limit of large on-site repulsion U_d , it was argued (34) that the resulting local kinematic (Umklapp) scattering depends only on effective single-band parameters, which are weakly dependent on doping. Indeed, photoemission experiments indicate a nearly material and doping independent near-nodal band structure characterized by a sizable Fermi velocity (v_F) on the arcs (30, 31).

For Landau's Fermi liquid, a quadratic temperature dependence of the resistivity is expected only at temperatures much smaller than the Fermi temperature. In the underdoped cuprates, $\rho \propto T^2$ extends to unusually high temperatures (Fig. 2) and is cut off at low temperature by either (non-universal) localization effects (6, 8) or superconducting fluctuations. We emphasize though that $\rho \propto T^2$ was extracted for YBCO ($p \approx 0.11$) down to low temperature (~ 4 K) (Fig. 3B) through the suppression of superconductivity in a high magnetic field (9), and that the corresponding value of $A_{2\Omega}$ falls on the universal plots of Figs. 4E&F. Due to the large value of $v_F \approx 2$ eVÅ on the arcs, both $k_B T$ and the energy scale associated with Umklapp scattering might be small compared to the single-particle energy scale $v_F K_a$, where K_a is the Fermi arc length (SOM f). This might account for the observation of a quadratic resistivity up to rather high temperature. As shown in Fig. 1A, for Hg1201 at temperatures below T^{**} the mean-free path is considerably larger than the planar lattice constant, thus the Ioffe-Regel criterion (42) for a good metal is satisfied (SOM g). The observation of quantum oscillations in YBCO appears to provide additional support for a Fermi-liquid state in the underdoped cuprates (43), although it is not clear if this particular phenomenon is a result of the presence of Cu-O chains in YBCO, and hence non-universal. Stronger evidence comes from the well-known T^2 dependence of the Hall angle (SOM e) (5). Nevertheless, the situation is highly unconventional, as exemplified by the presence of arcs, and by the evidence for a quantum critical point at p^* . Interestingly, recent NMR results imply a two-component local magnetic susceptibility, one temperature independent above T_c , i.e. Fermi-liquid-like, and the other temperature dependent and correlated with the formation of the pseudogap (44), which supports a two-fluid picture. In order to further test if the underdoped cuprates are, in effect, Fermi liquids, additional experiments can be envisaged. In particular, it will be important to check if optical conductivity measurements yield the quadratic frequency dependence expected for a Fermi liquid in samples in which the pure $\rho \propto T^2$ behavior is demonstrated from dc transport.

Figure 5 shows the updated phase diagram of the cuprates. Figure 5A focuses on the non-superconducting properties, neglecting complications (Fig. 5B) related to low structural

symmetry, disorder and localization effects (6, 8, 23), the ‘stripe-order’ anomaly near $p \approx 1/8$ (45), and inhomogeneities near p^* (11). The pseudogap temperature T^* has been associated with a transition to a state with translational-symmetry preserving magnetic order in both YBCO and Hg1201 (18). The coincidence of T^{**} with the onset of the polar Kerr-effect in YBCO (22) raises the possibility that this temperature may be universally associated with a second phase transition above T_c . Although it has been suggested that the pseudogap opens below T^* , one can also envisage a scenario in which the novel magnetic order at T^* does not gap the Fermi surface and the pseudogap develops as a result of broken crystal translational symmetry at T^{**} . There exist at least two qualitatively different scenarios near p^* that cannot yet be distinguished. Either both $T^*(p)$ and $T^{**}(p)$ approach zero at $p^* \approx 0.2$, the putative quantum critical point, or the two characteristic temperatures cross near optimal doping. A possible caveat is that even if much of the phase diagram is controlled by a quantum critical point, where $\rho \propto T$ is expected at all temperatures, this point may be inaccessible through the variation of physical parameters such as doping and magnetic field. Concerning the Fermi-liquid-like resistive behavior, even though the Fermi-surface undergoes a change in topology as it breaks up into arcs on the underdoped side of the phase diagram, the electronic scattering mechanism that gives rise to the dominant low-temperature quadratic behavior appears to be the same at the extreme doping levels of 1% and 33%.

We have demonstrated that the quadratic resistive regime at intermediate and low hole concentrations is a universal property of the cuprates, and that the structurally simple model compound Hg1201 exhibits a dramatic switch from T -linear to quadratic scattering rates upon cooling. Although the resistivity is highly sensitive to materials-specific characteristics, we have furthermore achieved a quantitative, universal understanding of both the linear and quadratic regimes by considering the resistance per principal building block, the copper-oxygen plaquette, of four structurally distinct cuprates. The analysis of materials-specific deviations from this underlying behavior can be expected to lead to profound insights into the non-universal features exhibited by individual materials. Most importantly, the present work provides a quantitative basis for the development of a comprehensive theoretical understanding of these fascinating materials.

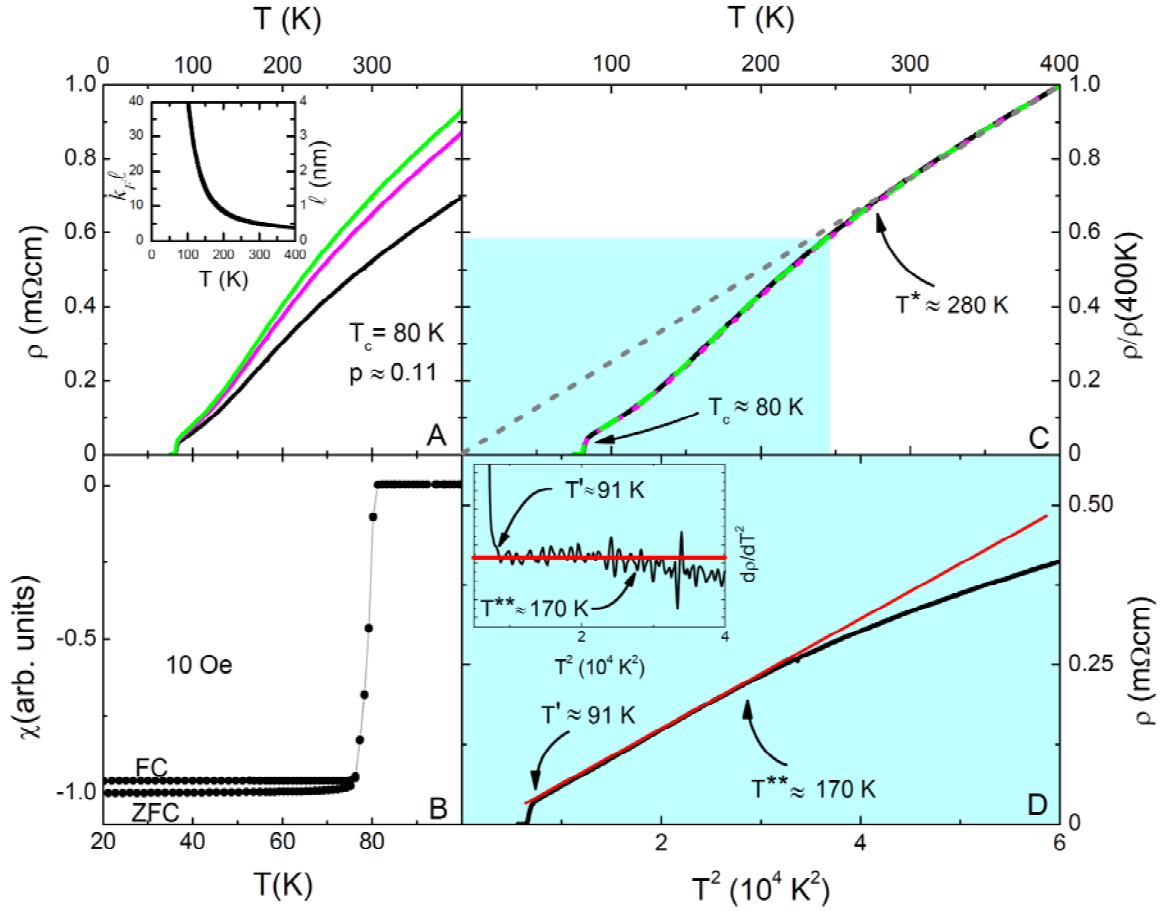


Fig. 1. *ab*-plane dc-resistivity and magnetic susceptibility for underdoped Hg1201 ($T_c = 80$ K). (A) Resistivity as a function of temperature for three samples. Inset: estimates of mean free path (l) and $k_F l$ (SOM f). (B) Magnetic susceptibility (zero-field-cooled (ZFC) and field-cooled (FC)) for one of the samples after its preparation for resistivity measurements (SOM c) reveals a sharp T_c of 80 K. The FC/ZFC ratio is 97%, indicative of very high sample quality (16). (C) When normalized at 400 K, the data in A) collapse onto a single curve, indicating high bulk homogeneity. High-temperature linear behavior, $\rho = \rho_0 + A_1 T$ (dashed line), with $\rho_0 \approx 0$ and $T^* \approx 280$ K. (D) The resistivity exhibits a quadratic temperature dependence between $T' \approx 90$ K and $T^{**} \approx 170$ K. This is also seen from the plot of $d\rho/d(T^2)$ (inset). Red lines are guides to the eye. Horizontal and vertical ranges correspond to blue area in C).

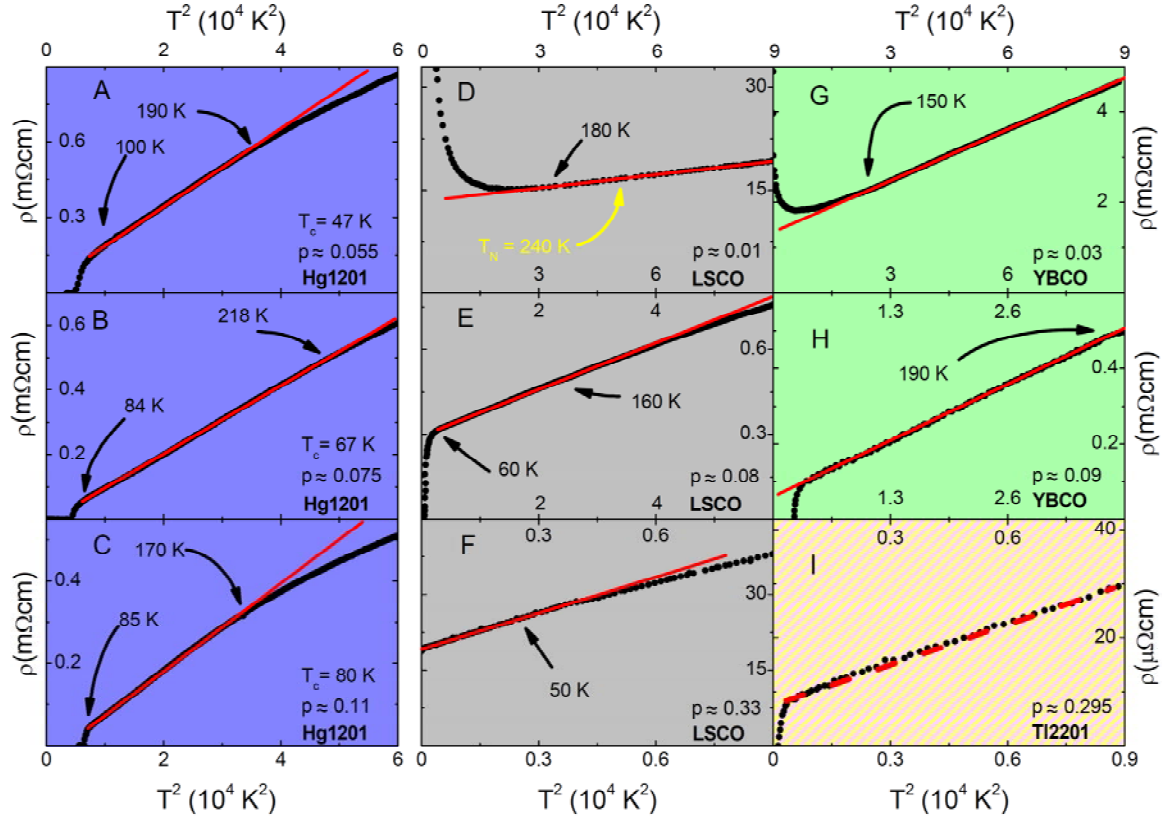


Fig. 2. Doping and compound dependence of T^2 -resistivity. (A to C) Quadratic resistivity in underdoped Hg1201 at three doping levels, observed from $T' \approx T_c + 15$ K (above the superconducting ‘tail’ for samples with $T_c = 47$ K - see SOM c) up to T^{**} . (D) Similar behavior for LSCO is demonstrated (SOM d) for prior data at $p = 0.01$, where T^2 behavior persists into the Néel state ($T_N = 240$ K) (6). For LSCO, it was previously reported (5) for $p = 0.02$ (not shown) and (E) $p = 0.08$, and for (F) $p = 0.33$ (13). For YBCO in zero magnetic field, it was reported for (G) $p = 0.03$ (5) and (H) for $p = 0.09$ (7). (I) For TI2201 at $p = 0.295$, the resistivity increases more slowly than T^2 (black dotted curve is slightly concave with respect to the straight dashed red line), which implies the presence of a small linear contribution (10). Red lines are guides to the eye. Lower (T_{ρ}') and upper (T_{ρ}^{**}) temperatures at which resistivity begins to deviate from the quadratic behavior are indicated by arrows. See SOM c and SOM e for estimates of characteristic temperatures and hole concentrations, respectively.

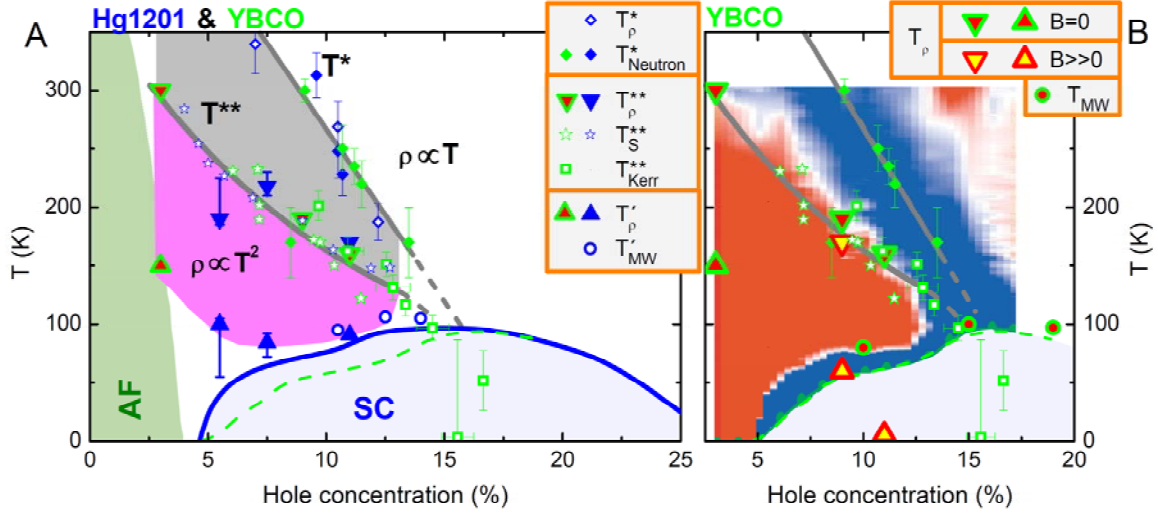


Fig. 3 **Phase diagram of Hg1201 and YBCO.** (A) Pseudogap temperature T^* , determined from deviation from linear- T resistivity (T^*_{ρ}) and neutron scattering (22) experiments (T^*_{Neutron}). Gray shaded area indicates the crossover to the quadratic regime (magenta) below T^{**} . The latter ends with the onset of SC fluctuations at T' , in agreement with microwave (T'_{MW}) measurements for Hg1201 (46) and YBCO (47), or when localization effects set in (around 150 K for YBCO at $p = 0.03$) (5). The temperatures of the TEP peak (T_S^{**}) for Hg1201 and YBCO and of the onset of the Kerr effect (T_{Kerr}^{**}) for YBCO track T^{**}_{ρ} from dc-resistivity. Blue and green symbols correspond to Hg1201 and YBCO, respectively. Green dashed line corresponds to the $T_c(p)$ of YBCO. Blue line is obtained from available data for $T_c(p)$ of Hg1201 (up to $p = 0.21$) (19) and extended to higher doping, as discussed in SOM e. Gray lines for $T^*(p)$ and $T^{**}(p)$ are guides to the eye. Antiferromagnetic (AF) phase is schematically indicated by the green shaded area. (B) The underlying T^2 (red contour) regime of YBCO is effectively captured by a map of the resistivity curvature (17). The quadratic resistive behavior is also apparent after applying a high magnetic field of $B \sim 50$ T (8, 9). For $p = 0.11$ (9), the applied field was sufficiently high to completely suppress the superconductivity, and the quadratic resistive behavior was observed to low temperature.

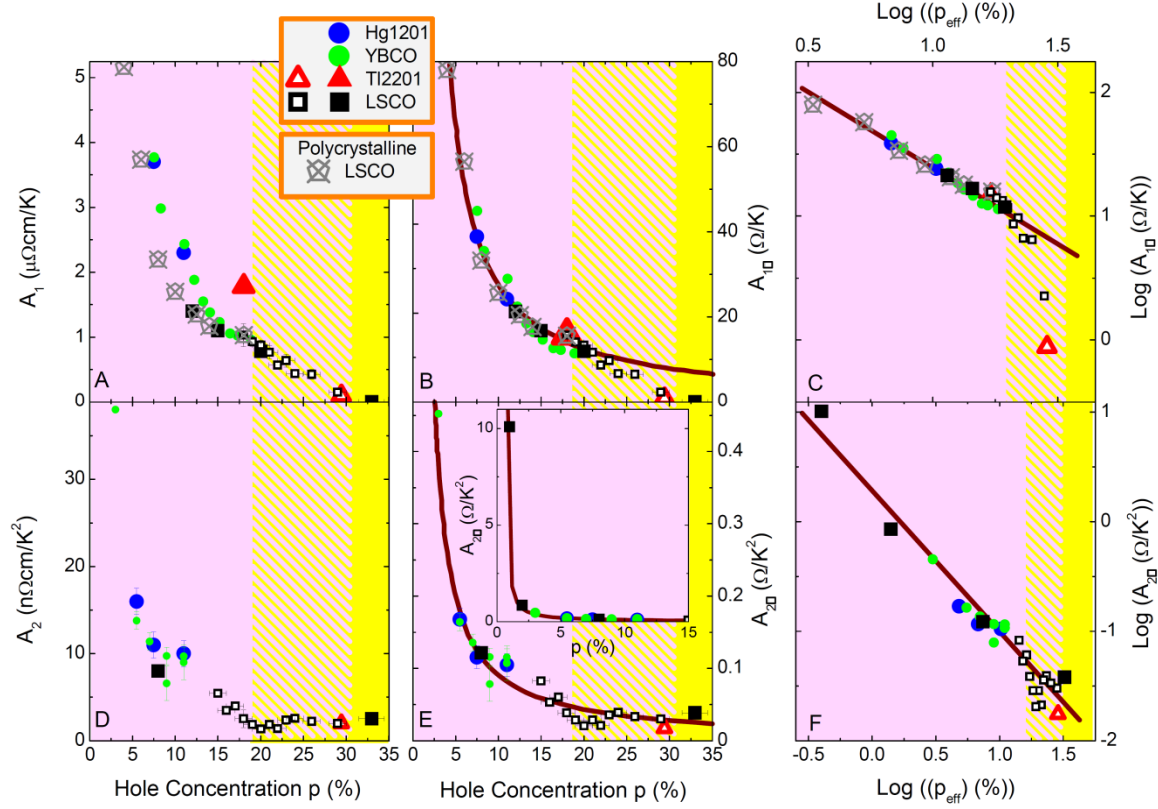


Fig. 4 Doping dependence of coefficients A_1 , $A_{1\Box}$, A_2 , and $A_{2\Box}$. There exist three distinct regimes: (i) for $p < 0.19$ (pink), either $\rho \propto A_1 T$ ($T > T^*$) or $\rho \propto A_2 T^2$ ($T^{**} > T > T^*$) is observed (filled symbols); (ii) for $0.19 \leq p \leq 0.3$ (pink/yellow hatched area), the resistivity (for LSCO and Tl2201) does not exhibit pure power-law behavior, and results from fits to $1/\rho = 1/(\rho_0 + A_1 T + A_2 T^2) + 1/\rho_{\max}$, rather than $\rho = \rho_0 + A_1 T + A_2 T^2$, are shown (open symbols). The two forms give closely similar results for A_1 , and for A_2 above $p = 0.25$, but not for A_2 near p^* (11); (iii) putative Fermi-liquid regime for $p > 0.3$ (below about 50 K) (yellow). (A, D) A_1 and A_2 versus hole concentration p . (B, E) Universal behavior of plaquette resistance coefficients $A_{1\Box}$ and $A_{2\Box}$, with approximately constant ratio $A_{1\Box}/A_{2\Box} \approx 325$ K for $p < 0.19$. (C, F) Log-log plots demonstrate the $1/p$ dependencies. A somewhat better fit is obtained with effective hole concentrations, $A_{1\Box}(p_{\text{eff}}) \propto 1/(p-p_1)$ (for $0.04 \leq p \leq 0.19$) and $A_{2\Box}(p_{\text{eff}}) \propto 1/(p-p_2)$ ($0.01 \leq p \leq 0.33$), with $p_1 = p_2 = 0.007(2)$. For LSCO, data for polycrystalline samples (12) are rescaled by factor of $1/5.5$ to match single crystal data.

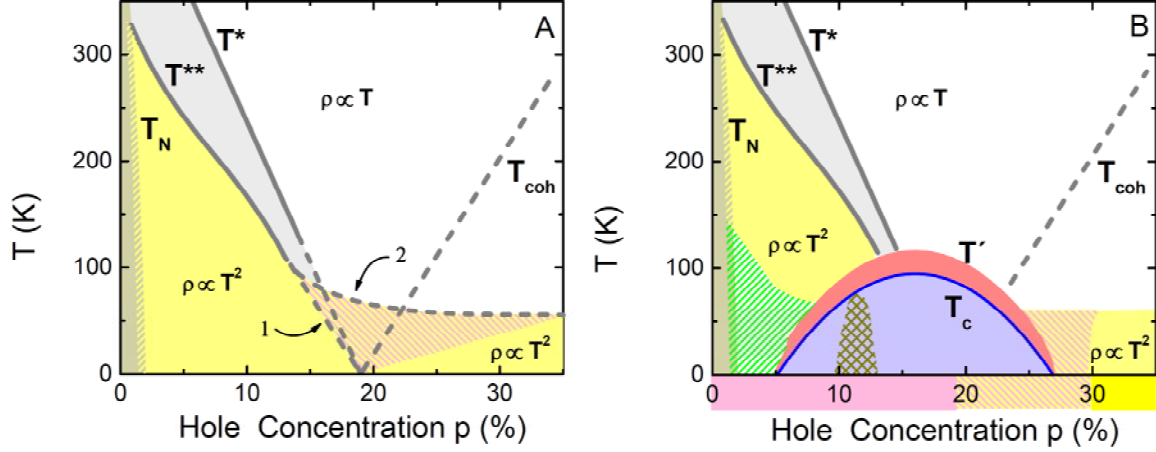


Fig. 5 **Modified phase diagram of the cuprates.** Phase diagram (A) without and (B) with disorder, superconductivity and “1/8” anomaly. The undoped cuprates are Mott (charge-transfer) insulators. (A) Antiferromagnetic (AF) order below T_N extends to nonzero doping. Quadratic resistive behavior (observed in LSCO even at $p = 0.01$, for $T > 150$ K) extends into the AF region. The ground state may be insulating up to a small, nonzero hole concentration. $T^*(p)$, and possibly also $T^{**}(p)$ mark phase transitions. T_{coh} corresponds to the loss of antinodal quasiparticle coherence, as observed in photoemission experiments (10). Two scenarios for $T^{**}(p)$ are indicated by arrows in A): $T^{**}(p)$ either approaches zero at the putative quantum critical point at $p^* \approx 0.19$ or crosses $T^*(p)$ and Fermi-liquid-like behavior is always present (hatched area). (B) Superconducting phase: blue; doping/temperature range of the superconducting fluctuations (46, 47): red; localization effects (8): green; $p = 1/8$ anomaly (45): olive; chemical inhomogeneities (11) complicate the interpretation of data (for LSCO) immediately above p^* : orange. In B), the three regimes from Fig. 4 are marked along the horizontal axis by corresponding colors.

References

1. P. W. Anderson, The resonating valence bond state in La_2CuO_4 and superconductivity. *Science* **235**, 1196 (1987).
2. H. Alloul, T. Ohno, P. Mendels, ^{89}Y NMR Evidence for a Fermi-liquid behavior in $\text{YBa}_2\text{Cu}_3\text{O}_{6+x}$. *Phys. Rev. Lett.* **63**, 1700 (1989).
3. T. Timusk, B. Statt, The pseudogap in high-temperature superconductors: an experimental survey. *Rep. Prog. Phys.* **62**, 61 (1999).
4. T. Ito, K. Takenaka, S. Uchida, Systematic deviation from T -linear behavior in the in-plane resistivity of $\text{YBa}_2\text{Cu}_3\text{O}_{7-y}$: Evidence for dominant spin scattering. *Phys. Rev. Lett.* **70**, 3995 (1993).
5. Y. Ando, Y. Kurita, S. Komiya, S. Ono, K. Segawa, Evolution of the Hall coefficient and the peculiar electronic structure of the cuprate superconductors. *Phys. Rev. Lett.* **92**, 197001 (2004).
6. Y. Ando, A. N. Lavrov, S. Komiya, K. Segawa, X. F. Sun, Mobility of the doped holes and the antiferromagnetic correlations in underdoped high- T_c cuprates. *Phys. Rev. Lett.* **87**, 017001 (2001).
7. Y. S. Lee *et al.*, Electrodynamics of the nodal metal state in weakly doped high- T_c cuprates. *Phys. Rev. B* **72**, 054529 (2005).
8. F. Rullier-Albenque, H. Alloul, F. Balakirev, C. Proust, Disorder, metal-insulator crossover and phase diagram in high- T_c cuprates. *Europhys. Lett.* **81**, 37008 (2008).
9. D. LeBoeuf *et al.*, Lifshitz critical point in the cuprate superconductor $\text{YBa}_2\text{Cu}_3\text{O}_y$ from high-field Hall effect measurements. *Phys. Rev. B* **84**, 014507 (2011).
10. N. E. Hussey, What drives pseudogap physics in high- T_c cuprates? A view from the (resistance) bridge. *J. Phys. Chem. Solids* **72**, 529 (2011).
11. R. A. Cooper *et al.*, Anomalous criticality in the electrical resistivity of $\text{La}_{2-x}\text{Sr}_x\text{CuO}_4$. *Science* **323**, 603 (2009).
12. T. Nakano *et al.*, Magnetic properties and electronic conduction of superconducting $\text{La}_{2-x}\text{Sr}_x\text{CuO}_4$. *Phys. Rev. B* **49**, 16000 (1994).
13. S. Nakamae *et al.*, Erratum: Electronic ground state of heavily overdoped nonsuperconducting $\text{La}_{2-x}\text{Sr}_x\text{CuO}_4$. *Phys. Rev. B* **79**, 219904 (2009).

14. Y. C. Ma, N. L. Wang, Infrared scattering rate of overdoped $Tl_2Ba_2CuO_{6+\delta}$. *Phys. Rev. B* **73**, 144503 (2006).
15. X. Zhao *et al.*, Crystal growth and characterization of the model high-temperature superconductor $HgBa_2CuO_{4+\delta}$. *Adv. Mater.* **18**, 3243 (2006).
16. N. Barišić *et al.*, Demonstrating the model nature of the high-temperature superconductor $HgBa_2CuO_{4+\delta}$. *Phys. Rev. B* **78**, 054518 (2008).
17. Y. Ando, S. Komiyama, K. Segawa, S. Ono, Y. Kurita, Electronic phase diagram of high- T_c cuprate superconductors from a mapping of the in-plane resistivity curvature. *Phys. Rev. Lett.* **93**, 267001 (2004).
18. Y. Li *et al.*, Unusual magnetic order in the pseudogap region of the superconductor $HgBa_2CuO_{4+\delta}$. *Nature* **455**, 372 (2008).
19. A. Yamamoto, W. Hu, S. Tajima, Thermoelectric power and resistivity of $HgBa_2CuO_{4+\delta}$ over a wide doping range. *Phys. Rev. B* **63**, 024504 (2000).
20. J.R. Cooper, J. W. Loram, Some correlations between the thermodynamic and transport properties of high- T_c oxides in the normal state, *J. Physique I* **6**, 2237 (1996).
21. J. R. Cooper, S. D. Obertelli, A. Carrington, J. W. Loram, Effect of oxygen depletion on the transport properties of $YBa_2Cu_3O_{7-\delta}$, *Phys. Rev. B* **44**, 12086 (1991).
22. A. Kapitulnik, J. Xia, E. Schemm, A. Palevski, Polar Kerr effect as probe for time-reversal symmetry breaking in unconventional superconductors. *New J. Phys.* **11**, 055060 (2009).
23. H. Eisaki *et al.*, Effect of chemical inhomogeneity in bismuth-based copper oxide superconductors. *Phys. Rev. B* **69**, 064512 (2004).
24. C. M. Varma, Pseudogap phase and the quantum-critical point in copper-oxide metals. *Phys. Rev. Lett.* **83**, 3538 (1999).
25. R. B. Laughlin, G. G. Lonzarich, P. Monthoux, D. Pines. The quantum criticality conundrum. *Adv. Phys.* **50**, 361 (2001).
26. L. P. Gor'kov, G. B. Teitel'baum, Mobility and its temperature dependence in underdoped $La_{2-x}Sr_xCuO_4$ interpreted as viscous motion of charges. *Phys. Rev. B* **77**, 180511(R) (2008).
27. D. N. Basov, T. Timusk, Electrodynamics of high- T_c superconductors. *Rev. Mod. Phys.* **77**, 721 (2005).

28. T. Yoshida, M. Hashimoto, I. M. Vishik, Z.-X. Shen, A. Fujimori, Pseudogap, superconducting gap, and Fermi arc in high- T_c cuprates revealed by angle-resolved photoemission spectroscopy. *J. Phys. Soc. Jpn.* **81**, 011006 (2012).
29. P. A. Lee, X.-G. Wen, Unusual superconducting state of underdoped cuprates, *Phys. Rev. Lett.* **78**, 4111 (1997).
30. X. J. Zhou *et al.*, High-temperature superconductors: Universal nodal Fermi velocity. *Nature* **423**, 398 (2003).
31. M. Hashimoto *et al.*, Doping evolution of the electronic structure in the single-layer cuprate $\text{Bi}_2\text{Sr}_{2-x}\text{La}_x\text{CuO}_{6+\delta}$: Comparison with other single-layer cuprates. *Phys. Rev. B* **77**, 094516 (2008).
32. R. Hlubina, T. M. Rice, Resistivity as a function of temperature for models with hot spots on the Fermi surface. *Phys. Rev. B* **51**, 9253 (1995).
33. J. Zaanen, Why the temperature is high. *Nature* **430**, 512 (2004).
34. S. Barišić, O.S. Barišić, Approaching large U_d high- T_c cuprates from the covalent side. *J. Supercond. Nov. Magn.* **25**, 669 (2012).
35. A. F. Bangura *et al.*, Fermi surface and electronic homogeneity of the overdoped cuprate superconductor $\text{Tl}_2\text{Ba}_2\text{CuO}_{6+\delta}$ as revealed by quantum oscillations. *Phys. Rev. B* **82**, 140501R (2010).
36. M. Platé *et al.*, Fermi surface and quasiparticle excitations of overdoped $\text{Tl}_2\text{Ba}_2\text{CuO}_{6+\delta}$ *Phys. Rev. Lett.* **95**, 077001 (2005).
37. C. Proust, E. Boaknin, R. W. Hill, L. Taillefer, A. P. Mackenzie, Heat transport in a strongly overdoped cuprate: Fermi liquid and a pure d-wave BCS superconductor. *Phys. Rev. Lett.* **89**, 147003 (2002).
38. M. M. J. French *et al.*, Tracking anisotropic scattering in overdoped $\text{Tl}_2\text{Ba}_2\text{CuO}_{6+\delta}$ above 100 K. *New J. Phys.* **11**, 055057 (2009).
39. N. Munnikes *et al.*, Pair breaking versus symmetry breaking: Origin of the Raman modes in superconducting cuprates. *Phys. Rev. B* **84**, 144523 (2011).
40. A. F. Santander-Syro *et al.*, Absence of a loss of in-plane infrared spectral weight in the pseudogap regime of $\text{Bi}_2\text{Sr}_2\text{CaCu}_2\text{O}_{8-\delta}$. *Phys. Rev. Lett.* **88**, 097005 (2001).
41. E. Gull, M. Ferrero, O. Parcollet, A. Georges, A. J. Millis, Momentum-space anisotropy and pseudogaps: A comparative cluster dynamical mean-field analysis of the

- doping-driven metal-insulator transition in the two-dimensional Hubbard model. *Phys. Rev. B* **82**, 155101 (2010).
42. A. F. Ioffe and A. R. Regel, Noncrystalline, amorphous and liquid electronic semiconductors. *Prog. Semicond.* **4**, 237 (1960).
43. D. LeBoeuf *et al.*, Electron pockets in the Fermi surface of hole-doped high- T_c superconductors. *Nature* **450**, 533 (2007).
44. J. Haase *et al.*, Two-component uniform spin susceptibility of superconducting $\text{HgBa}_2\text{CuO}_{4+\delta}$ single crystals measured using ^{63}Cu and ^{199}Hg nuclear magnetic resonance. *Phys. Rev. B* **85**, 104517 (2012).
45. S. A. Kivelson, *et al.* How to detect fluctuating stripes in the high-temperature superconductors. *Rev. Mod. Phys.* **75**, 1201 (2003).
46. M. S. Grbić *et al.*, Microwave measurements of the in-plane and c-axis conductivity in $\text{HgBa}_2\text{CuO}_{4+\delta}$: discriminating between superconducting fluctuations and pseudogap effects. *Phys. Rev. B* **80**, 094511 (2009).
47. M. S. Grbić *et al.*, Temperature range of superconducting fluctuations above T_c in $\text{YBa}_2\text{Cu}_3\text{O}_{7-\delta}$ single crystals. *Phys. Rev. B* **83**, 144508 (2011).

Acknowledgements

We gratefully acknowledge discussions with H. Alloul, S. Barišić, A.V. Chubukov, A. Georges, L.P. Gor'kov, S.A. Kivelson, D. van der Marel, F. Rullier-Albenque and A. Shekhter. The work at the University of Minnesota was supported by the Department of Energy, Office of Basic Energy Sciences. The work in Zagreb was supported by the Unity through Knowledge Fund. N.B. acknowledges support by the Alexander von Humboldt Foundation and through a Marie Curie Fellowship.

Supporting Online Material for

Universal plaquette resistance of the cuprate superconductors

N. Barišić,* Y. Li, G. Yu, X. Zhao, M. Dressel, A. Smontara, M. Greven*

* To whom correspondence should be addressed.

E-mail: nbarisic@ifs.hr (N.B.), greven@physics.umn.edu (M.G.)

This file includes:

SOM Text
Figs. S1 to S5
Table S1
References

Supplementary Text

(a) Resistivity and thermoelectric power

Starting from the Boltzmann equation, the conductivity $\sigma(T) = 1/\rho(T)$ and the thermoelectric power (TEP) $S(T)$ can be expressed in terms of the Fermi-Dirac distribution f , scattering rate $1/\tau$, and electron velocity v (48). For an electric field applied along the x direction, the conductivity is

$$\sigma_x = \frac{e^2}{4\pi^3\hbar} \iint \tau \frac{v_x^2}{v} da \frac{df}{dE} dE, \quad (1)$$

where the first integral is over a surface of constant energy E and the second integral is over all energies. The Fermi-Dirac distribution in a metal has an appreciable derivative only near the Fermi energy E_F , and contributions from states in the $k_B T$ energy window dominate. For example, in the case of a simple cubic crystal, Eq. (1) simplifies to

$$\sigma = \frac{e^2}{12\pi^3\hbar} \int \tau(k) v(k) da \quad (2)$$

where the velocity and scattering rate depend on the k -value of an electron. Not all the electrons near E_F contribute equally. In the cuprates, the antinodal regions of the Brillouin zone do not tend to contribute for electric fields applied along the CuO_2 planes.

The TEP is defined as the ratio between the thermal and charge currents,

$$S = \frac{\frac{1}{T} \text{thermal energy current}}{\text{charge current}} = \frac{\frac{1}{T} \int_0^\infty \sigma_x(E)(E-E_F)(df/dE)dE}{\int_0^\infty \sigma_x(E)(df/dE)dE} \quad (3)$$

where S is the Seebeck coefficient and, in accord with Eq. (1), the partial conductivity is

$$\sigma_x(E) = \frac{e^2}{4\pi^3\hbar} \int \tau \frac{v_x^2}{v} da. \quad (4)$$

For a metal, assuming only elastic scattering, this reduces to the Mott expression:

$$S = \frac{\pi^2}{3} \left(\frac{k_B}{e} \right) k_B T \left(\frac{\partial \ln \sigma(E)}{\partial E} \right)_{E=E_F} \quad (5)$$

It is evident that the TEP is closely related to the (charge) conductivity, and that both are dominated by the band structure in the $k_B T$ energy window around E_F . Consequently, both probes are sensitive to changes of the Fermi surface, which will manifest themselves in the temperature dependences of $\rho(T)$ and $S(T)$ as kinks, extrema, etc. Not every such a feature indicates a phase transition. However, when both dc-resistivity and TEP exhibit anomalies over large doping and temperature ranges, this cannot be accidental. Both observables feature striking universalities for different cuprates, indicating that the relevant parts of their Fermi surfaces are very similar.

The TEP of the cuprates can be qualitatively described as follows. At high temperatures, it exhibits linear behavior, $S(T) = S_0 + S_1 T$, with a mysterious (extrapolated) $T = 0$ intercept S_0 that becomes dramatically large in underdoped compounds. As the temperature is decreased, $S(T)$ exhibits a peak and a subsequent downturn, and finally falls to zero at T_c . Given that S should be zero at $T = 0$ (since the entropy is zero), the eventual downturn upon cooling is expected on general grounds.

The initial deviation from the high- T linear behavior of $S(T)$ appears to be correlated with $T^*(p)$ (19) and the maximum of $S(T)$ corresponds to $T^{**}(p)$. Both temperatures are strongly doping-dependent. Neutron diffraction experiments reveal $q = 0$ magnetic order at T^* in YBCO and Hg1201 (18), whereas Kerr-effect measurements give evidence for broken time-reversal symmetry at T^{**} in YBCO (22).

We note that several of our observations are in agreement with the extensive work undertaken by Honma and Hor (49). By analyzing results from numerous different experimental probes, they identified three characteristic temperatures above T_c , and the lower two correspond to T^* and T^{**} .

(b) Plaquette resistance

Given the quasi-two-dimensional nature of the cuprates, a natural but uncommon way to express the planar resistivity of bulk crystals is as resistivity per Cu-O plaquette, the building block of the planes. The remarkable universal scaling of $A_{1\Box}$ and $A_{2\Box}$ demonstrated in Fig. 4 for four structurally very different cuprates, including both single- and double-layer compounds, implies that the planar current flow is indeed dominated by the CuO_2 planes. For a three-dimensional metal, the resistivity is $\rho \equiv R a/l$, where R is the measured resistance, l the length along the direction of the current, and $area (a) = width (w) * thickness (t)$ the cross-sectional area perpendicular to the current. The sheet resistance $\rho_S = R w/l = \rho/t$, which like the resistance R has units of ohm (Ω), is a measure of the resistivity in the case of planar current flow in two-dimensional systems (such as thin films) of uniform thickness. For the cuprates, we consider the resistance per CuO_2 plane, $\rho_S = \rho/(c/n)$, where c is the c -axis lattice constant and n the number of CuO_2

planes per unit cell. One can further define the plaquette resistance as $\rho_{\square} = \rho_s/(a/b)$, where a and b are the planar lattice constants. For tetragonal Hg1201, $a = b$, and hence $\rho_{\square} = \rho_s$. For cuprates with lower structural symmetry, a and b differ at most by a few percent, and for simplicity we take $a = b$ in those cases as well.

(c) Experimental details and estimation of characteristic temperatures

Hg1201 single crystals were grown by a two-step flux method that yields underdoped samples (15). Three groups of crystals were subsequently annealed for several weeks under the following conditions: 520 °C in air, 460 °C in 0.1 Torr, and 550 °C at 10^{-6} Torr (16). This resulted in sharp transitions with $T_c = 80, 67,$ and 47 K, respectively. The samples were then cleaved to obtain ac -surfaces, on which gold wires (20 μm diameter) were attached with silver paste, subsequently cured for several minutes under the above respective annealing conditions, and then ‘quenched’ to room temperature. For the $T_c = 80$ K samples, this was a fairly simple task, since it was carried out at ambient pressure. In contrast, curing electrical contacts for the other two sets of samples was delicate, since they needed to be quickly introduced into, and then taken out from the furnace that maintained the low-pressure anneal conditions. Since the samples and the boat on which they were placed required some time to warm up and cool down, equilibrium conditions were never fully reached during the short curing time.

To exemplify the subtleties associated with the curing step, and to explain their consequences on our conclusions, the temperature dependences of the resistivity for four samples annealed to a T_c of 67 K are shown in Fig. S1A. To assure that curing did not change the bulk T_c , the magnetic susceptibility was subsequently measured (Fig. S1B). Although after the curing process the bulk transition remained centered at 67 K and sharp (the 10-90% characteristic falls within 1 K), the development of a small ‘tail’ is now observable toward higher temperatures (~ 80 K), indicating that a small fraction of the sample has a different (higher) hole concentration (Fig. S1B). This tail is observable in all three measurements: field cooled (FC), zero-field cooled (ZFC), and remnant moment (REM; field cooled, and then measured in zero applied field). The latter is particularly sensitive to inhomogeneities (16). The minority contribution affects the resistivity data in a subtle way. Due to filamentary superconductivity, T_c as measured by resistivity appears higher, and the T^2 regime is narrowed both from above and below, since contributions from the more highly doped minority regions exhibit both higher T' and lower T^{**} . This effect is the reason for the relatively large uncertainty in the extent of the $\rho \propto T^2$ regime for samples at the two lower hole concentrations (Fig. 3). We emphasize that the duration of the curing step is very short compared to the time required to significantly change the bulk oxygen (and hence hole) concentration, so that the vast majority of the sample volume is still at the targeted doping level. Consequently, the resistivity as a bulk probe is not significantly affected in the pure T -linear and quadratic regimes, and the coefficients A_1 and A_2 remain unchanged. We also note that the pseudogap temperature T^* , defined as the temperature below which the resistivity deviates from the high-temperature linear behavior, is about 350 K for the $T_c = 67$ K samples, consistent with the characteristic temperature determined from magnetic neutron scattering measurements of the onset of $q = 0$ magnetic order (18): the contributions from the more highly doped filamentary regions deviate from linearity at lower temperature than the bulk, and hence do not affect the determination of T^* . We conclude that the bulk doping level of our most underdoped

samples remains unchanged by the contact curing, and that the observed properties are intrinsic.

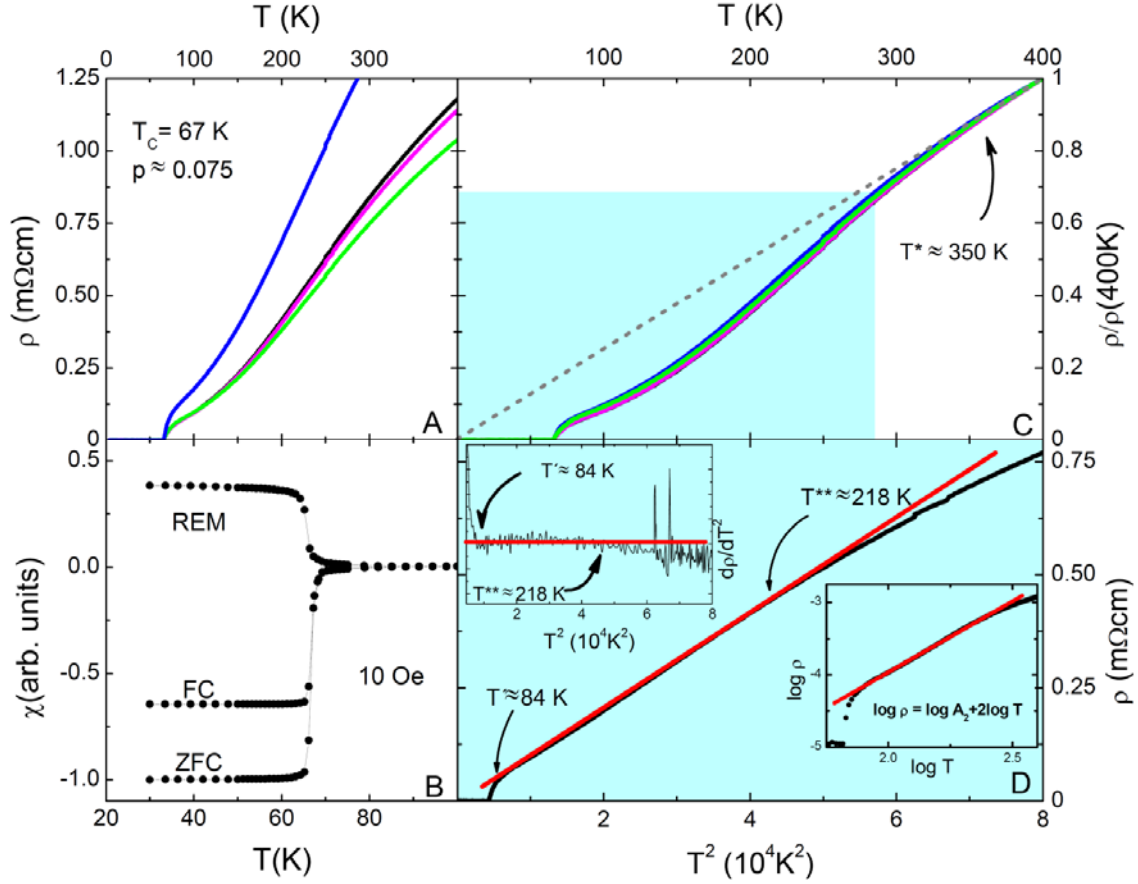


Fig. S1 Resistivity and magnetic susceptibility for underdoped Hg1201 ($T_c = 67$ K). (A) After annealing and contact curing (both performed in 0.1 Torr of air at a temperature of 460 °C), the *ab*-plane dc-resistivity was measured for four crystals. (B) Representative *c*-axis magnetic susceptibility data: zero-field-cooled (ZFC), field-cooled (FC) and remnant moment (REM). The ZFC/FC ratio is 65% and the REM is step-like, indicating good bulk sample quality and homogeneous oxygen distribution. (C) Data from A), normalized at the highest temperature (400 K), demonstrating data collapse (as in Fig. 1 for $T_c = 80$ K). $T^* \approx 350$ K is estimated from the high-temperature linear behavior ($\rho = \rho_0 + A_1 T$ with $\rho_0 \approx 0$), as indicated by the dashed line. (D) Representative resistivity data for one sample at lower temperature (corresponding to the blue region in B)) and $d\rho/d(T^2)$ (upper inset) vs. T^2 . Quadratic dependence, observed between $T' = 84$ K and $T^{**} = 218$ K, is also apparent from the $\log(\rho)$ vs. $\log(T)$ plot (lower inset).

T' and T^{**} demarcate the deviations from the quadratic behavior of the dc resistivity. To estimate these temperatures for Hg1201, four different approaches were compared: (1) Visual inspection of the ρ vs. T^2 curves (Figs. 1, 2 and S1). (2) Greater than 1% deviation of a parabolic fit from the data. A similar approach was also used to estimate T^* as the deviation from linear behavior. (3) The derivative $d\rho(T)/dT$ was calculated, and those data that fall on a line with zero intercept correspond to the pure T^2 regime. (4) The second derivative was calculated, as shown in insets of Figs. 1D and

S1D, and the characteristic temperatures were estimated from the deviation from a constant value larger than the error. All four approaches were found to result in the same characteristic temperatures within 10 K. For LSCO and YBCO, most of the corresponding characteristic temperatures were reported in the literature. When this was not the case, the reported data were digitized and the above approach was followed.

(d) Determination of coefficient A_2 for LSCO ($p = 0.01$)

The observation of a Fermi-liquid-like resistivity in the lightly-doped cuprates is surprising and was previously reported for LSCO at $p = 0.02$ (5). In Fig. S2, we demonstrate that this is the case even at $p = 0.01$ for previously reported data for LSCO (6).

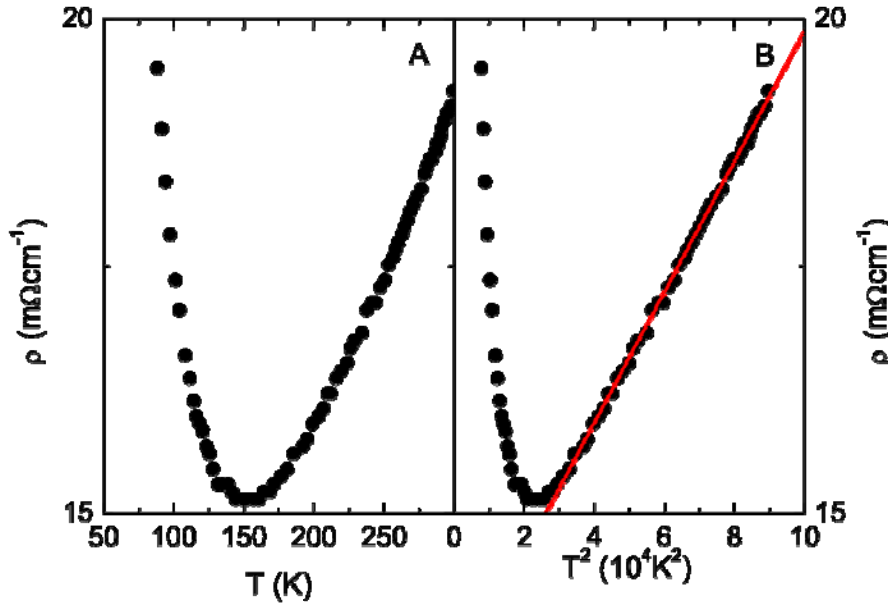


Fig. S2 Temperature dependence of the resistivity for very lightly doped LSCO ($p = 0.01$). (A) Resistivity up to room temperature, as reported in Ref. (6). (B) By plotting the resistivity versus T^2 , the quadratic regime is clearly revealed above ~ 170 K. The value $A_2 = 664 \text{ n}\Omega\text{cm}^{-1}\text{K}^{-2}$ is determined from a fit to the data at higher temperature to a parabolic dependence (red line). As noted before, the metallic behavior is insensitive to the onset of long-range antiferromagnetic order at $T_N = 240$ K (determined from a magnetization measurement), and the low-temperature upturn is due to the onset of localization (6).

(e) Phase diagrams of YBCO, LSCO and Bi2201

We show here that the main features of the phase diagrams of single-layer Hg1201 and double-layer YBCO discussed in the main text (Fig. 3) are also present in the structurally more complex lower- T_c compounds LSCO and Bi2201. We are not aware of planar resistivity data that reveal the quadratic resistive regime in Bi2201. For LSCO, the underlying universality is already apparent from the scaling of $A_{1\Box}(p)$ and $A_{2\Box}(p)$ demonstrated in Fig. 4. The observed universality leads to the conclusion that the Fermi surfaces of the cuprates must be essentially identical near the nodes. Furthermore, it gives insight into why the well-known empirical Presland-Tallon (PT) (50) formula and

Obertelli-Tallon-Cooper (OTC) relation (51) hold so well for different cuprate families; PT relate p to T_c , whereas OTC relate p to the TEP at 290 K.

For Hg1201, p is taken from the $T_c(p)$ relationship obtained in Ref. (19) (data available up to $p = 0.21$). For the previously measured compounds YBCO, LSCO, Bi2201 and Tl2201, we use the published hole concentration estimates. In all cases, either the PT formula or the OTC relation was used to determine the hole concentration. The superconducting dome of Hg1201 (thick blue line in Fig. 3) is extended on the overdoped side using the PT formula.

We use the contour plots of Ref. (17) as ‘background’ for the phase diagrams of YBCO (Figs. 3 and S3), LSCO (Fig. S4) and Bi2201 (Fig. S5), since they capture the various characteristic temperatures remarkably well. The contour plots were obtained by normalizing ab -plane dc-resistivity data at each doping level at high temperature, calculating the second derivative, and linearly interpolating the results at different doping levels. We find that $T^*(p)$ universally falls in the middle of the ‘blue’ region (which differs from the observations made in Ref. (17)), whereas the upper and lower boundaries of the red region in the underdoped regime correspond to T^{**} and T' , respectively.

Before considering the phase diagrams of the lower- T_c materials LSCO and Bi2201, we first add in Fig. S3 several experimental details to the phase diagram of YBCO (Fig. 3). The boundary of the antiferromagnetic phase was determined from zero-field μ SR (52). The Kerr effect indicates broken time-reversal symmetry in YBCO below T^{**} (22). At lower doping and temperatures slightly below T^{**} , magnetic neutron scattering experiments for YBCO provide indirect evidence for an ‘electronic liquid crystal’ (ELC) state, which was found to be affected by a magnetic field (53). It is not clear as yet if the ELC state is a universal property of the cuprates, or a phenomenon specific to YBCO. In the same temperature range (above $p = 0.05$) a feature has been found to appear around 450 cm^{-1} in the c -axis optical conductivity of YBCO (54). Although this feature was attributed to the Josephson plasmon, it is tempting to relate it to the onset of the ELC state due to its similar doping and temperature dependence. The sharp decrease of the characteristic temperature observed by optical conductivity at lower doping (54) coincides with the disappearance of superconductivity at $p = 0.05$ and with a change in the symmetry of the Raman response from B_{2g} to B_{1g} (55). Finally, T' attributed to the onset of superconducting fluctuations, as deduced from microwave conductivity (46, 47), falls exactly onto the lower boundary of the red surface in the contour plot, which in turn closely tracks $T_c(p)$. A similarly narrow fluctuation regime that tracks the superconducting dome and behaves rather classically was deduced from dc-resistivity measurements in high magnetic fields (56).

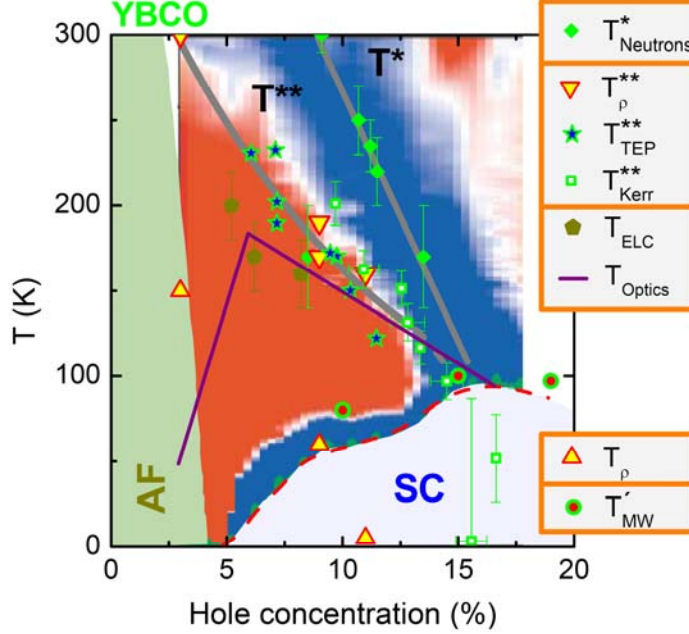


Fig. S3. **Phase diagram of YBCO with emphasis on experimental observations related to T^{**} .** The pseudogap temperature T^* lies in the middle of the blue region of the contour plot of Ref. (17) and extrapolates to zero temperature at $p \approx 0.19$ (upper gray line). T^* signifies a phase transition to a novel state of matter characterized by an unusual magnetic order that preserves the lattice translational symmetry (18). At $p = 0.085$, the ordering temperature was found to sharply decrease (57), to a value consistent with T^{**} rather than T^* . The upper boundary of the red region corresponds to T^{**} . Within error, T^{**} agrees with characteristic temperatures from TEP (20, 21), *ab*-plane dc resistivity (in zero (5, 7) and high (8, 9) magnetic fields), and Kerr effect (22). The latter result suggests that, at least in YBCO, T^{**} is therefore associated with a second phase transition above T_c . Below the slightly lower temperature T_{ELC} , evidence for an ‘electronic liquid crystal’ state has been found. This state appears to be further stabilized by a magnetic field (53). Above $p \approx 0.05$, coincident with the onset of superconductivity and a change in the symmetry of the Raman response (55), a feature appears around 450 cm^{-1} in the *c*-axis optical conductivity below T^{**} (54). The lower bound of the red area closely tracks the superconducting dome and corresponds to the onset of the superconducting fluctuations as determined by microwave conductivity (47). The upward triangles mark the lower limit of the T^2 behavior in the dc-resistivity in zero ($p = 0.03$) (5) and high magnetic fields ($p = 0.09, 0.11$) (8, 9). For $p = 0.09$, the quadratic behavior was not observed to very low temperature, presumably because the applied magnetic field was not strong enough to fully suppress superconducting fluctuations. The downward triangles mark the upper onset of the observed T^2 behavior.

The phase diagrams of LSCO and Bi2201 are even more complex than that of YBCO. LSCO and Bi2201 are single-CuO₂-layer compounds that feature lower structural symmetry, more disorder and a significantly lower value of T_c at optimal doping than simple tetragonal Hg1201 (23). Nevertheless, the characteristic temperatures (T^* , T^{**} , T' and T_c) appear in a very similar fashion on the respective contour plots of Ref. (17).

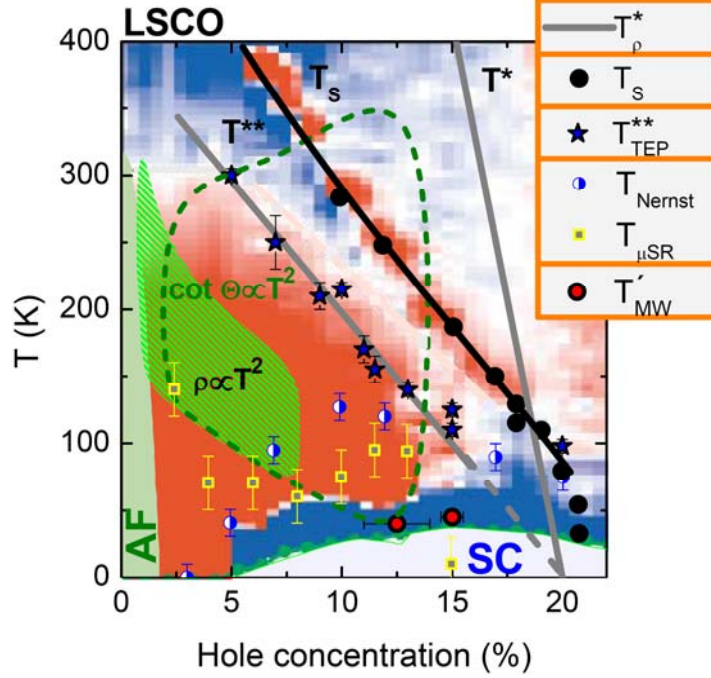


Fig. S4 **Phase diagram of LSCO.** T^* determined from dc-resistivity (61) falls in the middle of the blue/white region of the contour plot of Ref. (17). The well-known structural transition at T_S (62) modifies the transport properties in its vicinity and is clearly visible. As for YBCO, the upper boundary of the large red area corresponds to T^{**} as deduced from the peak in the TEP (58, 59). The temperature (T_{Nernst}), below which Nernst signal appears (60), approximately coincides at intermediate doping with the characteristic temperature from μSR measurements ascribed to charge localization effects (63). Also indicated is the onset of superconducting fluctuations as determined from microwave conductivity (67), as well as the regions in which $\rho \propto T^2$ and $\cot\theta_H \propto T^2$ have been observed (5). The planar resistivity features a quadratic resistivity at intermediate temperatures even at $p = 0.01$ (6) (SOM d).

LSCO exhibits a particularly high pseudogap temperature (61), which falls again into the middle of the blue/white region (Fig. S4). The compound undergoes a structural phase transition at T_S from body-centered tetragonal at high temperature to orthorhombic at lower temperature (62), which is clearly evident from the contour plot. A quadratic temperature dependence of the planar resistivity was previously reported for a relatively narrow doping ($p = 0.02 - 0.08$) and temperature ($T \approx 60 - 300$ K) range (5), much narrower than the red contour, which again is bound from above by T^{**} as determined from TEP. Interestingly, $T^{**}(p)$ lies parallel to $T_S(p)$. The pure $\rho \propto T^2$ behavior in LSCO is bound at high doping by a region in which a substantial Nernst signal (60), localization effects (from μSR (63) and dc-resistivity (8, 64)), and (non-universal) low-energy stripe correlations (near $p \approx 0.10 - 0.12$) (65) are observed. Whereas the $\rho \propto T^2$ behavior breaks down in this regime, this is not the case for the result $\cot\theta_H \propto T^2$ ($\cot\theta_H = \rho/R_H$, where R_H is the Hall coefficient), which was found to extend throughout a large part of the phase diagram of Fig. S4 (5), crossing T^{**} at high temperature and reaching T' at low temperature. In conventional metals, both quadratic temperature dependences signify Fermi-liquid behavior. Since ρ ($\propto 1/n\tau$) and R_H ($\propto 1/n$) are inversely proportional to the

effective carrier density (n), any change in the latter quantity is identically reflected in both observables, whereas the derived quantity $\cot\theta_H$ is solely proportional to the scattering rate ($1/\tau$). Therefore, in order to explain the reduced $\rho \propto T^2$ regime of LSCO, it is tempting to look for a scenario in which predominately the density of states is affected and the scattering rate in the near-nodal regions remain unchanged. LSCO exhibits considerable localization effects at low temperature and low hole concentrations, as evidenced by significant values of the residual resistivity (Fig. 2) and by the upturn of $T_{\mu\text{SR}}$ for $p < 0.07$ in Fig. S4 (8, 63, 64). Finally, we note that microwave-conductivity measurements indicate narrow superconducting fluctuation regime (66, 67), as for Hg1201 (46) and YBCO (47).

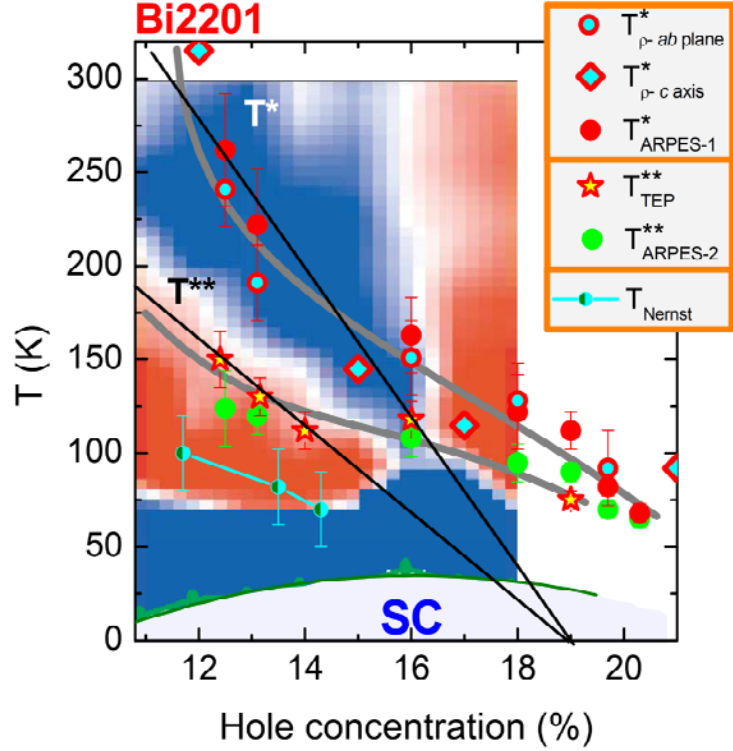


Fig. S5 **Phase diagram of Bi2201**. T^* is determined from ab -plane (71) and c -axis (68) resistivity as well as photoemission experiments (71). T^{**} corresponds to the peak in the TEP (69, 70) and to a second temperature observed by photoemission (71). Substantial Nernst signal is found to appear at an even lower temperature (60). Black and gray lines are guides to the eye.

The above considerations allow us to better understand the phase diagram of Bi2201 (Fig. S5). As for the other compounds, T^* in the underdoped region (deduced from both ab -plane and c -axis resistivity in this case) falls in the middle of the blue region of the contour plot, and the upper onset of the red region in the underdoped regime corresponds to the peak in the thermoelectric power (69, 70). A recent photoemission experiment (71) revealed the existence of two distinct temperature scales which agree well with T^* and T^{**} . Although in Ref. (71) the lower temperature was attributed to the onset of pair formation, other scenarios can be envisaged that involve charge-density-wave formation, nematic order, etc. Given the observation of a Kerr effect in YBCO, the

characteristic temperature T^{**} might indeed be universally associated with a phase transition. In fact, the recent observation of a Kerr effect together with supporting evidence from ARPES and nonlinear optical measurements in nearly optimally doped Pb-Bi2201 ($\text{Pb}_{0.55}\text{Bi}_{1.5}\text{Sr}_{1.6}\text{La}_{0.4}\text{CuO}_{6+\delta}$) seem to support this scenario (72). However, near optimal doping, the values of T^* and T^{**} are very similar, making it difficult to distinguish the signatures associated with these two characteristic temperatures.

The red contour for underdoped Bi2201 is relatively narrow when compared to YBCO and LSCO. Its lower edge is matched well by the onset of the Nernst signal, which can be attributed either to the superconducting fluctuations (60) or, as discussed above, to the onset of a separate ordering tendency. $T^*(p)$ and $T^{**}(p)$ at lower doping extrapolate linearly to zero around $p = 0.19$ (black lines), as in the other compounds. On the other hand, in the overdoped regime, Bi2201 exhibits a much more gradual doping tendency (grey lines), and both characteristic temperatures remain above the superconducting dome.

An interesting question is why the contour plots of Ref. (17) capture so well the various characteristic temperatures of YBCO, LSCO and Bi2201, and in particular the underlying quadratic resistive regime. The plots were obtained by normalizing the resistivity data at each doping level by the respective 300 K (400 K in the case of LSCO) value, and by subsequently taking the second derivative of the normalized curves with respect to temperature. The normalization temperatures lie above T^{**} and, in some cases, even above T^* . At 300-400 K, the (extrapolated) values of A_1T and A_2T^2 are rather similar. Therefore, normalization approximately corresponds to dividing all the curves by $1/p$, since $A_1 \propto A_2 \propto 1/p$. Consequently, in the doping and temperature range where the underlying resistivity is quadratic in temperature, the normalized second derivative is a constant (red areas). For YBCO and LSCO, the lower and upper bounds of these areas in the superconducting doping regime correspond to T' and T^{**} , respectively. The structural transition of LSCO is also clearly observed since it introduces an additional scattering mechanism.

(f) Estimate of energy scale $v_F K_a$ at $p = 0.01$ doping

In the underdoped cuprates, the Fermi-liquid-like quadratic resistivity extends to surprisingly high temperatures. We speculate here that this might be the result of a relatively large single-particle energy scale, $v_F K_a$, which in the case of the truncated Fermi surface (arcs) takes on the role of the Fermi energy E_F . Here, K_a is the doping-dependent nodal Fermi arc length (27, 29, 73, 74) and v_F the Fermi velocity on the arcs. In a Fermi-liquid, $1/\tau \propto T^2$ is attributed to electronic Umklapp scattering. Due to the large value of $v_F \approx 2 \text{ eV}\text{\AA}$ determined from photoemission (30, 75), both $k_B T$ and the energy scale associated with effective Umklapp scattering might be small compared to $v_F K_a$, even though K_a decreases with decreasing doping.

We provide a simple estimate of this energy scale for the extreme case of $p = 0.01$. The underlying Fermi surface is approximated by a circle of circumference $2\pi k_F$, with $k_F \approx \pi/a$, where $a \approx 3.9 \text{ \AA}$ is the planar lattice constant. We use the photoemission estimates of K_a for Bi2212 listed in Table S1 (74). We assume $T_c = 95 \text{ K}$ at optimal doping and use the PT formula (50) to estimate the hole concentration p . Linear extrapolation suggests that $\sim 5\%$ of the Fermi surface remains ungapped at $p = 0.01$. The

resultant single-particle energy scale $v_F K_a = 2 \text{ eV} \text{ \AA} \cdot 0.05 (2\pi^2/3.9 \text{ \AA}^{-1}) \approx 0.5 \text{ eV}$ is indeed much larger than $k_B T \sim 0.025 \text{ eV}$ at room temperature.

P	T_c	K_a (%)
0.11	UD75	28
0.14	UD92	33
0.20	OD86	44

Table S1 Fermi-arc length for underdoped and overdoped Bi2212 (74).

(g) Estimate of mean-free path

The large scattering rate and the high temperature up to which the quadratic resistivity is observed in the underdoped cuprates would seem to suggest that the Fermi-liquid concept has no validity (76, 77). A key requirement for a good metal is that the mean free path l is larger than the lattice constant ($a \sim 4 \text{ \AA}$ in the case of the cuprates). Starting from Ohm's law,

$$\sigma_{CuO_2} = \frac{1}{\rho_{CuO_2}} = \frac{ne^2 \tau_e(T)}{m} \quad (6)$$

writing $\tau_e(T) = \ell / v_F = m \ell / \hbar k_F$, and assuming a parabolic dispersion in two dimensions ($n = k_F^2 / 2\pi$), the conductivity can be written as

$$\sigma_{CuO_2} = \frac{e^2}{2\pi\hbar} (k_F \ell). \quad (7)$$

The product $k_F \ell$ of the Fermi wave vector and the mean free path is a dimensionless number and turns out to be considerably larger than 1 in the temperature range of interest (up to $\sim 200 \text{ K}$). This is shown in the inset of Fig. 1a. Using the average Fermi vector of $k_F \approx \pi/a \approx 1 \text{ \AA}^{-1}$ associated with the unreconstructed Fermi surface, we estimate the mean free path at T^{**} to be approximately 10 \AA , above the Ioffe-Regel limit. Similarly, it was estimated for overdoped Tl2201 (78) and LSCO (13) that $l \approx 150 \text{ \AA}$ below 100 K . Nevertheless, in the T -linear regime at higher temperatures, the mean free path eventually becomes smaller than the lattice constant, crossing the Ioffe-Regel limit if the Fermi velocity is assumed to be isotropic. However, the simplest interpretation of our data in the quadratic (and also T -linear) regime is that the predominant effect of doping on the resistivity is the reduction of the number of charge carriers ($\rho \propto 1/p$), while the (corresponding) scattering rate is unchanged. If we consider the possibility that the cuprates remain 'nodal' metals even above T^* , i.e., that only a fraction (proportional to p) of the states at the Fermi level contribute to the planar transport, it follows that even at high temperatures this limit is not crossed.

SOM references

48. J. S. Dugdale, The electrical properties of metals and alloys. Edward Arnold, London, 1977.
49. T. Honma, P. H. Hor, Unified electronic phase diagram for hole-doped high- T_c cuprates. *Phys. Rev. B* **77**, 184520 (2008).
50. R. Presland, J.L. Tallon, R.G. Buckley, R.S. Liu, N.E. Flower. General trends in oxygen stoichiometry effects on T_c in Bi and Tl superconductors. *Physica C* **176**, 95 (1991).
51. S. D. Obertelli, J. R. Cooper, J. L. Tallon, Systematics in the thermoelectric power of high- T_c oxides. *Phys. Rev. B* **46**, 14 928 (1992).
52. F. Coneri, S. Sanna, K. Zheng, J. Lord, R. De Renzi, Magnetic states of lightly hole-doped cuprates in the clean limit as seen via zero-field muon spin spectroscopy. *Phys. Rev. B* **81**, 104507 (2010).
53. D. Haug *et al.*, Neutron scattering study of the magnetic phase diagram of underdoped $\text{YBa}_2\text{Cu}_3\text{O}_{6+x}$. *New J. Phys.* **12**, 105006 (2010).
54. A. Dubroka *et al.*, Evidence of a precursor superconducting phase at temperatures as high as 180 K in $\text{RBa}_2\text{Cu}_3\text{O}_{7-\delta}$ (R = Y;Gd;Eu) superconducting crystals from infrared spectroscopy. *Phys. Rev. Lett.* **106**, 047006 (2011).
55. L. Tassini, W. Prestel, A. Erb, M. Lambacher, R. Hackl, First-order-type effects in $\text{YBa}_2\text{Cu}_3\text{O}_{6+x}$ at the onset of superconductivity. *Phys. Rev. B* **78**, 020511(R)(2008).
56. F. Rullier-Albenque, H. Alloul, G. Rikken, High-field studies of superconducting fluctuations in high- T_c cuprates: Evidence for a small gap distinct from the large pseudogap. *Phys. Rev. B* **84**, 014522 (2011).
57. V. Baledent *et al.*, Evidence for competing magnetic instabilities in underdoped $\text{YBa}_2\text{Cu}_3\text{O}_{6+x}$. *Phys. Rev. B* **83**, 104504 (2011).
58. K. Kumagai *et al.*, Magnetic order and suppression of superconductivity around $x=0.12$ in $\text{La}_{2-x}\text{Sr}_x\text{CuO}_4$ and $\text{La}_{2-x}\text{Ba}_x\text{CuO}_4$. *Physica C* **235**, 1715 (1994).
59. J. S. Kim, B. H. Kim, D. C. Kim, Y.W. Park, Two pseudogap behavior in $\text{La}_{2-x}\text{Sr}_x\text{CuO}_4$: Thermoelectric power at high temperature. **17**, 151 (2004).

60. Y. Wang, L. Li, N. P. Ong, Nernst effect in high- T_c superconductors. *Phys. Rev. B* **73**, 024510 (2006).
61. J. L. Tallon *et al.*, Critical doping in overdoped high- T_c superconductors: a quantum critical point? *Phys. Stat. Sol. (b)* **215**, 531 (1999).
62. K. Yamada *et al.*, Doping dependence of the spatially modulated dynamical spin correlations and the superconducting-transition temperature in $\text{La}_{2-x}\text{Sr}_x\text{CuO}_4$. *Phys. Rev. B* **57**, 6165 (1998).
63. I. Watanabe *et al.*, Change of the dynamics of internal fields in the normal state of $\text{La}_{2-x}\text{Sr}_x\text{CuO}_4$ observed by muon-spin-relaxation. *J. Phys. Soc. Jpn.* **77**, 124716 (2008).
64. G. S. Boebinger *et al.*, Insulator-to-metal crossover in the normal state of $\text{La}_{2-x}\text{Sr}_x\text{CuO}_4$ near optimum doping. *Phys. Rev. Lett.* **77**, 5417 (1996).
65. J. M. Tranquada, B. J. Sternlieb, J. D. Axe, Y. Nakamura, S. Uchida, Evidence for stripe correlations of spins and holes in copper oxide superconductors. *Nature* **375**, 561 (1995).
66. L. S. Bilbro *et al.*, Temporal correlations of superconductivity above the transition temperature in $\text{La}_{2-x}\text{Sr}_x\text{CuO}_4$ probed by terahertz spectroscopy. *Nat. Phys.* **7**, 298 (2011).
67. M. S. Grbić *et al.*, Universally narrow superconducting fluctuation regime in the cuprates. *In preparation*.
68. A. N. Lavrov, Y. Ando, S. Ono, Two mechanisms of pseudogap formation in Bi-2201 : Evidence from the c -axis magnetoresistance. *Europhys. Lett.* **57**, 267 (2002).
69. T. Kondo *et al.*, Contribution of electronic structure to thermoelectric power in $(\text{Bi,Pb})_2(\text{Sr,La})_2\text{CuO}_{6+\delta}$. *Phys. Rev. B* **72**, 024533 (2005).
70. Y. Dumont, C. Ayache, G. Collin, Dragging excitation characteristics from thermoelectric power in $\text{Bi}_2(\text{Sr}_{2-y}\text{La}_y)\text{CuO}_{6+\delta}$ single crystals. *Phys. Rev. B* **62**, 622 (2000).
71. T. Kondo *et al.*, Disentangling Cooper-pair formation above the transition temperature from the pseudogap state in the cuprates. *Nat. Phys.* **7**, 21 (2011).
72. R. -H. He *et al.*, From a single-band metal to a high-temperature superconductor via two thermal phase transitions. *Science* **331**, 1579 (2011).

73. M. Oda, R. M. Dipasupil, N. Momono, M. Ido, Hyperbolic dependence of $2\Delta_0$ vs. e_c ratio on hole-doping level in high- T_c cuprates: energy scale in determining e_c . *J. Phys. Soc. Jpn.* **69**, 983 (2000).
74. W. S. Lee *et al.*, Abrupt onset of a second energy gap at the superconducting transition of underdoped Bi2212. *Nature* **450**, 81(2007).
75. I. M. Vishik *et al.*, ARPES studies of cuprate Fermiology: superconductivity, pseudogap and quasiparticle dynamics. *New J. Phys.* **12**, 105008 (2010).
76. V. J. Emery, S.A. Kivelson, Superconductivity in bad metals. *Phys. Rev. Lett.* **74**, 3253 (1995).
77. O. Gunnarsson, M. Calandra, J. E. Han, Colloquium: Saturation of electrical resistivity. *Rev. Mod. Phys.* **75**, 1085 (2003).
78. N. E. Hussey *et al.*, Angular dependence of the c -axis normal state magnetoresistance in single crystal $Tl_2Ba_2CuO_6$. *Phys. Rev. Lett.* **76**, 122 (1995).